RESEARCH ARTICLE



Isotropic turbulence apparatus with a large vertical extent

Davis W. Hoffman¹ • John K. Eaton¹

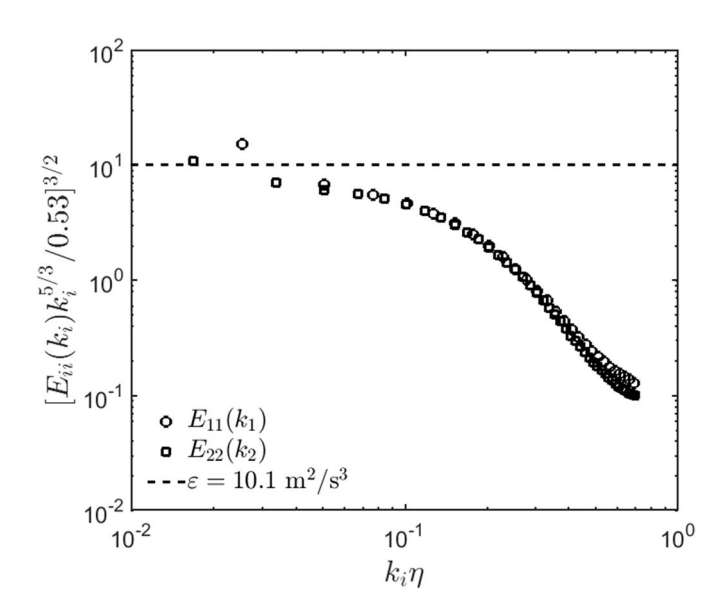
Received: 26 June 2021 / Revised: 7 September 2021 / Accepted: 16 September 2021 / Published online: 28 September 2021 © The Author(s), under exclusive licence to Springer-Verlag GmbH Germany, part of Springer Nature 2021

Abstract

An experimental flow facility for sustaining a column of nearly isotropic turbulence in air has been developed. Four arrays of synthetic jet actuators are arranged along the walls of a vertical tower, producing a homogeneous region spanning 13 integral length scales in the vertical direction. The isotropy, homogeneity, and various turbulence properties are quantified using optical measurement techniques. At the highest jet power setting, a root-mean-square velocity of 0.73 m/s and a Reynolds number Re_{λ} of 240 are attained. Although the mean flows are not negligible, their contribution to the turbulence kinetic energy production is insignificant, given the small magnitude of the measured Reynolds stress. The flow exhibits a high degree of isotropy when comparing the longitudinal autocorrelation functions, although some anisotropy is observed in the large scales according to the rms velocity ratio, which ranges from 0.90 to 1.33 over the measured regions. Despite these deviations from ideal isotropic turbulence, the experimental design is well-suited for the study of inertial particle agglomeration during gravitational settling.

Graphical abstract







[☐] Davis W. Hoffman dwhoff@stanford.edu

Stanford University, Department of Mechanical Engineering, Stanford, CA, USA

209 Page 2 of 11 Experiments in Fluids (2021) 62:209

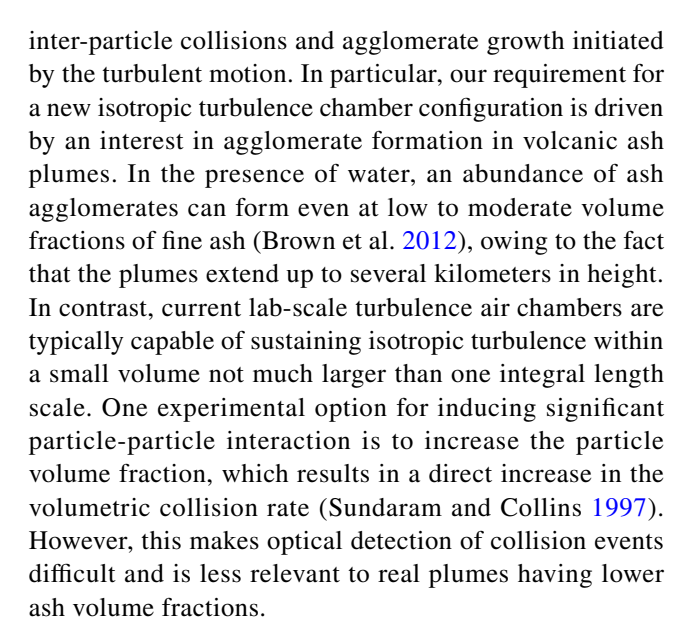
1 Introduction

In recent years, there have been numerous applications for lab-scale experiments capable of generating highly energetic turbulence with minimal mean velocity and shear. In most canonical and naturally occurring turbulent flows, including duct flows, jets, wakes, and boundary layers, the turbulent energy is derived from mean shear stresses. The mean velocities in these flows can obfuscate the measurement of important turbulence quantities, especially when using optical techniques. Isotropic turbulence, on the other hand, is an idealized flow that has no mean velocity gradients (Pope 2000), making it ideal for probing the fundamental behavior of turbulence.

Various approaches for approximating isotropic turbulence have been taken, and the experimental designs vary according to the intended purpose. Historically, the most conventional method employs a wind tunnel to produce grid-generated turbulence (Comte-Bellot and Corrsin 1966), but the uniform mean flow and the decay of turbulence kinetic energy (TKE) downstream of the grid are often viewed as undesirable features of the flow. This can be circumvented by using oscillating grids in a closed liquid chamber (De Silva and Fernando 1994), but the method is less practical for gases when high Reynolds numbers are desired. Hwang and Eaton (2004) produced nearly isotropic turbulence in a closed air chamber by replacing the oscillating grids with synthetic jet actuators mounted to the corners of a cubical box aimed at a common point at the center of the chamber. This method achieved high Reynolds numbers and a sufficient degree of isotropy when compared to grid-forcing methods.

Since then, further improvements to the isotropy in these turbulence box designs have been made by constructing chambers in various polyhedral shapes, including both regular and truncated icosahedron shapes (Zimmermann et al. 2010; Dou et al. 2016) similar in form to a soccer ball. Besides the study of Lagrangian properties of turbulence (Zimmermann et al. 2010), the general design has also been used to quantify the modified settling velocity of inertial particles (Good et al. 2014), evaporation rate of droplets (Goepfert et al. 2010), and sediment suspension in granular beds (Johnson and Cowen 2020). In one notable study, Bellani and Variano (2014) showed that a high degree of isotropy could be obtained even with parallel planar arrays of round jets submerged in a water tank, with the homogeneous region extending more than an integral length scale in all directions from the tank's center.

While previous experiments have explored the dynamics of inertial particles in isotropic turbulence for the dilute limit, where particle-particle interactions are rare, there is a need for new experiments that can quantify the effects of



In this paper, we present a new experimental design for an isotropic turbulence tower that sustains a larger turbulence volume than existing experiments of its kind. Although the experiment is designed to study inertial particles as they agglomerate through the isotropic region of the turbulence, the focus of the present paper is to characterize and document the underlying flow behaviors and offer suggestions for the design of future turbulence chambers.

2 Experimental setup

2.1 Facility overview

The turbulence tower under consideration was conceived as a hybridization of the icosahedron configuration of Dou et al. (2016) and Zimmermann et al. (2010) with the planar jet configuration of Bellani and Variano (2014) and Carter et al. (2016). Top, side, and section views of the turbulence tower are depicted in Fig. 1. Turbulence is produced by synthetic jet actuators arranged along the outer chamber walls. The tower itself takes the form of an octagonal prism, where four of the walls support the jet actuators, and the remaining walls provide optical access.

A single synthetic jet assembly, depicted in Fig. 2, consists of a 4 inch woofer (loudspeaker) flange-mounted to the outer chamber wall along with a spacer plate, allowing the woofer cone to vibrate freely. Air is cycled through a jet orifice of diameter $d_j = 16$ mm, which is centered with the woofer axis, generating a chain of vortex rings that propagates toward the center of the chamber. A threaded drain hole located below the main jet orifice serves to remove any particles or debris that accumulate in the bottom of the synthetic jet cavity over time. During normal



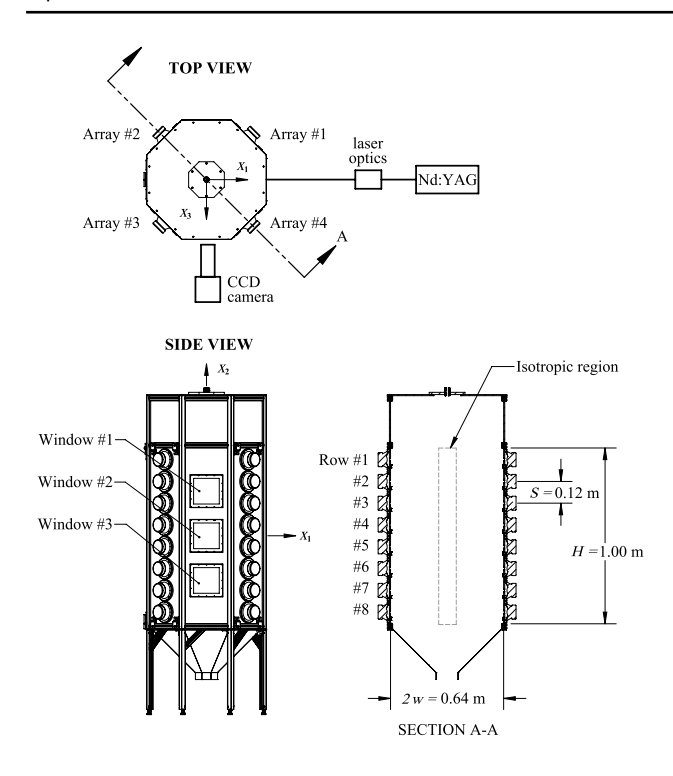


Fig. 1 Schematic of turbulence tower as viewed from the top, side, and an oblique section that passes through the center

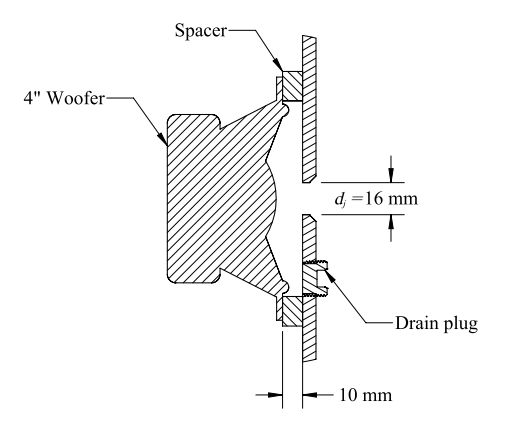


Fig. 2 Section view of the synthetic jet actuator assembly

operation, the drain hole is plugged so as not to interfere with the operation of the jet.

Each woofer is powered by a sinusoidal signal having voltage amplitude between 3.5 and 5.5 V and assigned frequency between 70 and 76 Hz. The signal for each frequency is produced by one of four analog function generators, before it is amplified and distributed to the woofers. The amplifier channels are configured such that no set of opposing jets share the same frequency, to avoid the formation of standing pressure waves and periodic flow structures at the center of the tower. The specific arrangement

Table 1 Arrangement of speaker frequencies (in Hz) for all 32 jets

Row #				
Array #	1	2	3	4
1	70	72	74	76
2	72	74	76	70
3	74	76	70	72
4	76	70	72	74
5	70	72	74	76
6	72	74	76	70
7	74	76	70	72
8	76	70	72	74

of frequencies organized by jet array and row number is provided in Table 1.

In all experiments, the frequency assignment is kept the same, but the voltage applied equally to all woofers is varied to change the turbulence intensity in the tower. The power consumed by all of the jets combined varies between 12 and 29 W depending on the supplied voltage amplitude. The woofer response is relatively flat in the range of 70-76 Hz, so the power consumption is approximately uniform across individual jets.

2.2 Design considerations

The overall dimensions of the tower are chosen to provide an acceptable degree of homogeneity and the largest range of turbulence length scales as possible. First, the vertical inter-jet spacing *S* should be minimized and is limited by the woofer outer diameter. A consequence of the geometry is that a primary stagnation point forms at the center of each row of jets. If the distance between jet rows is too large, secondary stagnation points can also form at intermediate locations between the primary stagnation points. Moreover, the dimension *S* dictates the amount of shear around each stagnation point which, if too large, can cause anisotropy in the turbulent fluctuations.

Similarly, the tower half-width w should be sufficiently large to allow the jet turbulence to spread before reaching the center of the tower. A guideline for choosing w involves matching the jet half-width $r_{1/2}(x)$ at a distance x = w from the jet orifice with one half of the inter-jet spacing S.

$$r_{1/2}(x=w) \approx Aw \approx \frac{S}{2}$$
 (1)

In Eq. (1), A is the spreading rate of the jet. For simplicity, we substitute $A \approx 0.094$, a value typically used for continuous turbulent jets (Pope 2000). From this, we obtain an estimate of w = 64 cm. As a practical consideration, the estimate for w made here should be interpreted as an upper bound, since the spreading rate of opposed synthetic jets is likely larger than 0.094.



The scaling argument made by Dou et al. (2016), given by Eq. (2), indicates that an increase in chamber size would also lead to an increase in microscale Reynolds number Re_{i} ,

$$Re_{\lambda} \sim N_j^{1/4} \sqrt{U_j w/\nu},$$
 (2)

where U_j is the mean velocity produced by the jets, and N_j is the total number of jets. This scaling relies on the assumption that the integral length scale L is proportional to w. A more appropriate scaling is $L \sim d_j$, since any flow structures much larger than d_j can be ascribed to mean secondary flows within the chamber. The replacement of w with d_j in Eq. (2) leads to a new scaling,

$$Re_{\lambda} \sim N_j^{1/4} \sqrt{Re_j},$$
 (3)

where $Re_j = U_j d_j / v$ is the jet Reynolds number. The rate of flow work relates to the power applied to the jet actuator P through an efficiency factor η_i .

$$\eta_j P = \frac{1}{2} \rho \left(\frac{\pi}{4} d_j^2 \right) U_j^3 \tag{4}$$

Then the Reynolds number scaling with P can be written as

$$Re_{\lambda} \sim N_j^{1/4} \left(\eta_j d_j P \right)^{1/6}. \tag{5}$$

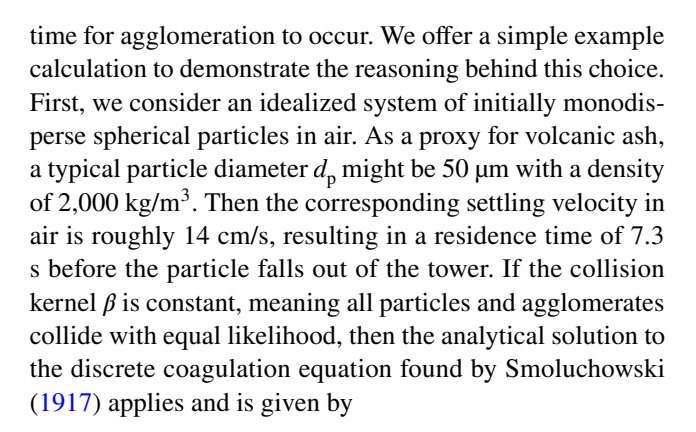
Equation 5 is most useful when the actuator efficiency η_j is constant. Then changes in P can be made to control Re_{λ} in the tower. In general, the actuator efficiency is an unknown function of the applied power, frequency, and jet diameter, and so, the scaling must be used with caution.

Though no significant influence of w on Re_{λ} is expected, the chamber width does play a major role in setting the Kolmogorov length scale η . Since the dissipation rate is proportional to the rate of flow work generated by the jet actuators and inversely proportional to the chamber volume, it follows that

$$\eta = \left(\frac{v^3}{\varepsilon}\right)^{1/4} \sim \frac{w^{1/2}}{(\eta_i P)^{1/4}}.\tag{6}$$

Thus, choosing w too large will lead to an undesired increase in Kolmogorov length scale and a narrowing of the inertial subrange. Based on the dimensions of prior turbulence chambers that achieved a broad inertial subrange, we chose a tower half-width of w = 32 cm. This choice in w is notably less than the guideline of 64 cm given before, so some trade-off between the dissipation value and the degree of homogeneity is expected.

The height of the turbulence region H is the most flexible design parameter. Since the motivation behind the turbulence tower is for the study of inertial particle agglomeration, we chose H = 1 m to allow sufficient particle residence



$$n_k(t) = \frac{n_1(0) \left[\frac{1}{2}\alpha\beta t n_1(0)\right]^{k-1}}{\left[1 + \frac{1}{2}\alpha\beta t n_1(0)\right]^{k+1}}.$$
 (7)

In Eq. (7), $n_k(t)$ represents the number of agglomerates per unit volume that contain k parent particles at some later time t starting from an initial number density of $n_1(0)$. The parameter α is the sticking probability. We assume $\alpha \approx 0.5$, meaning any given collision has an equal probability of resulting in either agglomeration or rebound.

The collision kernel β can be estimated using the theory developed by Saffman and Turner (1956) for inertialess particles,

$$\beta = \sqrt{\frac{8\pi}{15}} \frac{\varepsilon}{\nu} d_{\rm p}^3, \tag{8}$$

where ν is the air kinematic viscosity. Taking $\varepsilon \approx 10 \text{ m}^2/\text{s}^3$, the collision kernel evaluates to $\beta \approx 1.3 \times 10^{-10} m^3 s$.

If we define the agglomerate probability function $P_k(t)$ as the population of an aggregate class k normalized by the total population, Smoluchowski's solution from Eq. (7) can be recast as

$$P_k(t) \equiv \frac{n_k(t)}{\sum_{k=1}^{\infty} n_k(t)} = \frac{\left[\frac{1}{2}\alpha\beta t n_1(0)\right]^{k-1}}{\left[1 + \frac{1}{2}\alpha\beta t n_1(0)\right]^k}.$$
 (9)

Letting the particle volume fraction be 5.0×10^{-5} , equivalent to an initial number density of $n_1(0) = 3.8 \times 10^8 m^{-3}$, and substituting all other values into Eq. (9), the fraction of the total population contained in the unagglomerated class k=1 after exposure to the turbulence is $P_1(t=7.3 \text{ s})=0.84$. In other words, 16% of the final population is contained in an aggregate class ($k \ge 2$).

This estimate indicates that a significant amount of agglomeration can occur in the short time that the particles reside in the turbulence. Factors that are left out of this simplified analysis, such as differential settling and finite particle inertia effects, would enhance agglomeration even



further. One additional advantage to the turbulence tower design is that the height H can be extended to any desired value without having to fabricate a new experiment from scratch.

2.3 PIV measurements

Two-dimensional and two-component velocity fields are obtained near the central axis of the tower using particle image velocimetry (PIV). Three windows, labeled #1, #2, and #3 from top to bottom (see Fig. 1), allow optical access to the flow at different vertical sections of the tower. To evaluate homogeneity, measurements are made on the x_1 - x_2 plane at all three window locations, as well as on the x_1 - x_3 plane at the window #2 location. For conciseness, all results shown correspond to measurements taken on the x_1 - x_2 plane at the location of window #2, unless otherwise stated.

Aerosolized olive oil, produced by six Laskin nozzles, is used as a flow tracer. The tracer droplets, approximately 1 µm in size, are injected into the tower from above for roughly 1 s while the synthetic jets are turned on. The jets remain on for at least 30 s before measurement to allow secondary flows generated by tracer injection to dissipate. The dispersed tracers are then illuminated by a New Wave Solo III-15 dual-pulse Nd:YAG laser with a wavelength of 532 nm.

The scattered light is recorded on a TSI model 630094 CCD camera with a 6600×4400 pixel array and 5.5 µm pixel size. The camera is equipped with an AF Micro-Nikkor 200 mm lens and an aperture setting of f/8, resulting in an object resolution of 7.6 µm and a field of view of 50.2×33.5 mm. The inter-frame time is adjusted between 40 and 60 µs, depending on the woofer power setting, to allow an average tracer displacement of at least 5 pixels between frame pairs. For a comprehensive list of PIV parameters used over all experiments, see Table 2.

The PIV images are post-processed using an iterative cross-correlation algorithm. The final interrogation window size is 32x32 pixels with 50% overlap, corresponding to a

 Table 2
 List of PIV parameters

Laser sheet thickness	0.52 mm
Inter-frame time	40-60 μs
Sample rate	1.45 Hz
Lens focal length	200 mm
Lens aperture	<i>f</i> /8
Camera resolution	7.6 µm/pixel
Field of view	$50.2 \times 33.5 \text{ mm}$
IR size	32×32
Vector spacing (50% overlap)	122 μm
Image pairs acquired	1000

vector spacing of 122 μ m. A consistency filter is used to detect spurious vectors, which removed less than 0.8% of the velocity data points. Interpolation is used in place of the spurious vectors when computing velocity power spectra and two-point correlations. When the yield rate of any given realization is less than 95%, the corresponding image pair is removed from the calculation. Low yield rates typically arise from aliasing and decorrelation caused by high energy eddies and strong velocity gradients. Since fewer than 2% of image pairs are removed from the datasets for this reason, the resulting bias in the dissipation rate estimation is found to be no more than about 5%.

Individual tracer particles are typically captured in images by 2-4 adjacent pixels and can cause a bias in the correlation peak locations towards integer values, or "peak-locking". To alleviate this problem, a histogram equalization approach proposed by Roth and Katz (2001) is applied to the velocity datasets. The displacement correction is 0.02 pixels on average.

3 Results

Turbulence quantities at each jet power setting are extracted from PIV constructed velocity fields. A summary of these quantities after the appropriate ensemble and spatial averaging is given in Table 3. The quantities in the first four numeric columns correspond to the single measurement made at window #2, whereas the 5-95 percentile range given in the far right column is obtained from an aggregate of all measurements, including each window location. A complete discussion of how the turbulence quantities are computed is contained in Sects. 3.1 and 3.2.

Table 3 Summary of turbulence quantities at each jet power. The first four numeric columns give the spatial average at the window #2 measurement location. The range, listed on the far right column, represents the 5-th and 95-th percentile of spatial deviations over all measurement locations for the 29 W case

Power (W)	12	20	24	29	Spatial deviation
$u_{1,\text{rms}}/u_{2,\text{rms}}$	1.03	1.01	1.00	1.00	0.90-1.33
$ \langle u_1 \rangle /u_{1,\text{rms}}$	0.17	0.08	0.14	0.16	0.01-0.42
$ \langle u_2 \rangle /u_{2,\text{rms}}$	0.14	0.20	0.15	0.18	0.01-0.37
$ \langle u_1'u_2'\rangle /u_{1,\text{rms}}\cdot u_{2,\text{rms}}$	0.14	0.08	0.05	0.04	0.00-0.15
$q^2 (m^2/s^2)$	0.28	0.84	1.23	1.62	81-133%
$\varepsilon (\mathrm{m^2/s^3})$	0.6	4.0	6.8	10.1	87-138%
$\eta (\mu m)$	269	171	149	135	92-104%
τ_{η} (ms)	4.8	1.9	1.5	1.2	85-107%
λ_f (mm)	8.1	5.6	5.2	4.9	86-110%
Re_{λ}	165	198	222	240	81-114%
L (mm)	81.7	68.3	70.8	71.9	72-126%



Recognizing the symmetry of the jet forcing about the x_2 axis, a weighted average is used to calculate the generic scalar property χ given the property in the x_1 and x_2 direction, χ_1 and χ_2 , respectively.

$$\chi = \frac{2}{3}\chi_1 + \frac{1}{3}\chi_2 \tag{10}$$

In addition, we adopt the notation $\langle \cdot \rangle$ for the ensemble averaging operator and $\overline{\cdot}$ for the spatial averaging operator. Then the time-averaged and fluctuating parts of the velocity can be defined as $\langle u_i \rangle$ and $u_i' = u_i - \langle u_i \rangle$, respectively.

3.1 Single-point velocity statistics

Velocity statistics are recorded over a duration of about 12 minutes. The sampling rate is small enough to ensure the samples are uncorrelated, and the statistics are found to be time-stationary. Vector plots of a single instantaneous velocity field and the time-averaged velocity field are shown in Fig. 3. The instantaneous field exhibits strong fluctuations without any visible net flow across the frame, while the time-averaged field exhibits mean shear around a secondary stagnation point, which is located towards the right side of the frame.

Velocity data are assembled over all points in space and all PIV realizations to construct PDFs. The PDFs of velocity fluctuation, shown in Fig. 4, are similar and approximately Gaussian distributed, indicating no skewness towards a preferred direction in any of the velocity components. One quantitative metric for evaluating the large scale isotropy is the root-mean-square (rms) velocity ratio $u_{1,\rm rms}/u_{2,\rm rms}$ given in Table 3. The ratio is close to unity, when spatially averaged across the window #2 location, regardless of the jet power setting. However, there is considerable spatial deviation in this value, as measured for the 29 W case. Near the primary stagnation point, the horizontal fluctuations are most pronounced, leading to rms velocity ratios as high as 1.33. In the vicinity of the secondary stagnation points, the ratio can drop as low as 0.90.

The time-averaged velocity fields are small in comparison to the fluctuating velocities as quantified by the ratio $|\langle u_i \rangle|/u_{i,\text{rms}}$. These values are larger than 0.10 for nearly all measurements, listed in Table 3, and no trend with respect to the jet power setting is observed. We conclude that although the mean flow is only a fraction of the fluctuating component, the effect on the turbulence statistics cannot be neglected without further investigation.

In ideal isotropic turbulence, the off-diagonals of the Reynolds stress tensor are exactly zero, or $\langle u_i'u_j'\rangle=0$ for $i\neq j$. The only off-diagonal Reynolds stress component that can be obtained from the measured 2D velocity fields is $\langle u_1'u_2'\rangle$. To quantify the degree to which the velocity components are

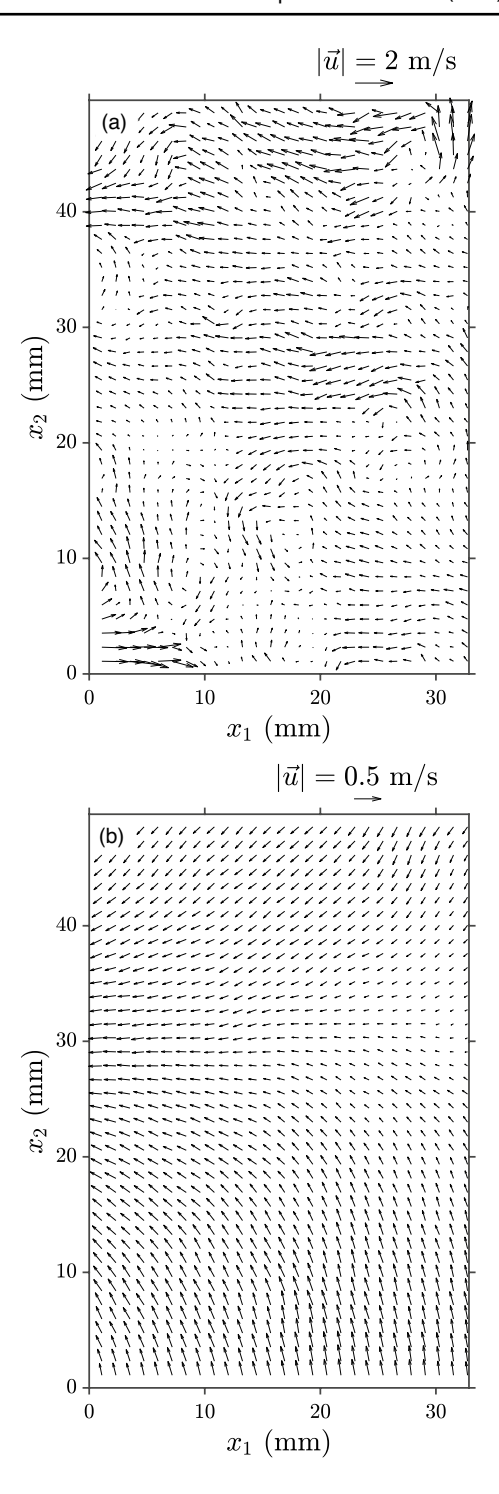


Fig. 3 a Instantaneous and **b** time-averaged velocity fields on the x_1 – x_2 plane at 29 W jet power. For clarity, every 10-th vector from the original dataset is shown. Note the difference in vector scale between the two plots

correlated, the normalized Reynolds stress $|\langle u'_1 u'_2 \rangle| u_{1,\text{rms}} \cdot u_{2,\text{rms}}$ is computed and reported in Table 3. Note that the absolute value is taken before spatial averaging, so that a symmetric distribution of the velocity correlation



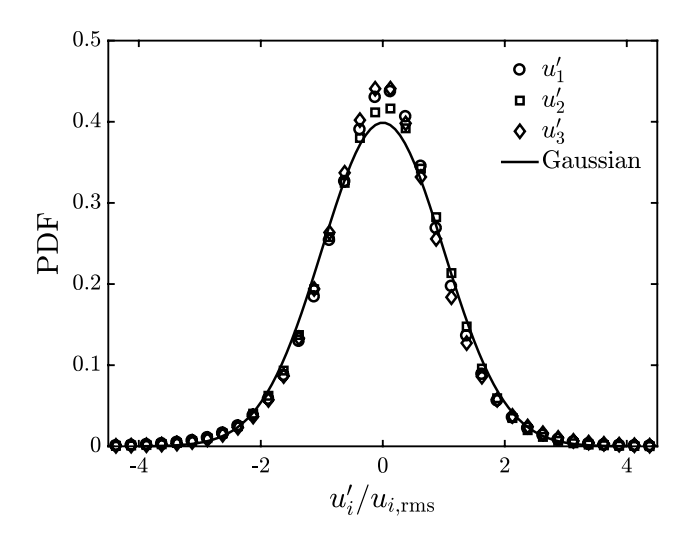


Fig. 4 Normalized velocity PDFs from the 29 W jet power experiments

about zero will not necessarily result in a small value. The normalized Reynolds stress decreases as the jet power increases and is less than 0.10 for applied powers of 20 W and above.

Although the velocity components are found to be only very weakly correlated, it is possible that the production of TKE, $-\langle u_i'u_i'\rangle\partial\langle u_i\rangle\partial x_i$, could be significant given the mean shear that exists around the stagnation points. One of the production terms, $-\langle u_1'u_2'\rangle \partial \langle u_1\rangle \partial x_2$, is plotted in Fig. 5 for the 29 W jet power setting. The spatial variation of this quantity is somewhat exagerrated due to the effect of measurement noise on the mean velocity gradient and could be reduced further by increasing the total number of samples. However, the ratio of TKE production to dissipation averaged over space evaluates to $-\varepsilon^{-1}\langle u_1'u_2'\rangle \partial \langle u_1\rangle/\partial x_2 = 0.0074$. The other measurable production term evaluates t o $-\varepsilon^{-1}\langle u_2'u_1'\rangle \partial \langle u_2\rangle/\partial x_1 = -0.0020$. This result provides strong evidence that the mean shear contributes little to the TKE at the center of the tower.

The Kolmogorov length scale η and time scale τ_{η} are computed as

$$\eta = \left(\frac{v^3}{\varepsilon}\right)^{1/4}, \tau_{\eta} = \left(\frac{v}{\varepsilon}\right)^{1/2}. \tag{11}$$

The dissipation rate is maximum for the 29 W power setting, for which $\eta = 136 \, \mu \text{m}$ and $\tau_{\eta} = 1.2 \, \text{ms}$.

The quantity q^2 , or twice the turbulence kinetic energy, is estimated by assuming $u_{3,\mathrm{rms}} \approx u_{1,\mathrm{rms}}$, given the symmetry of the tower.

$$q^2 = u_{i,\text{rms}} u_{i,\text{rms}} \approx 2u_{1,\text{rms}}^2 + u_{2,\text{rms}}^2$$
 (12)

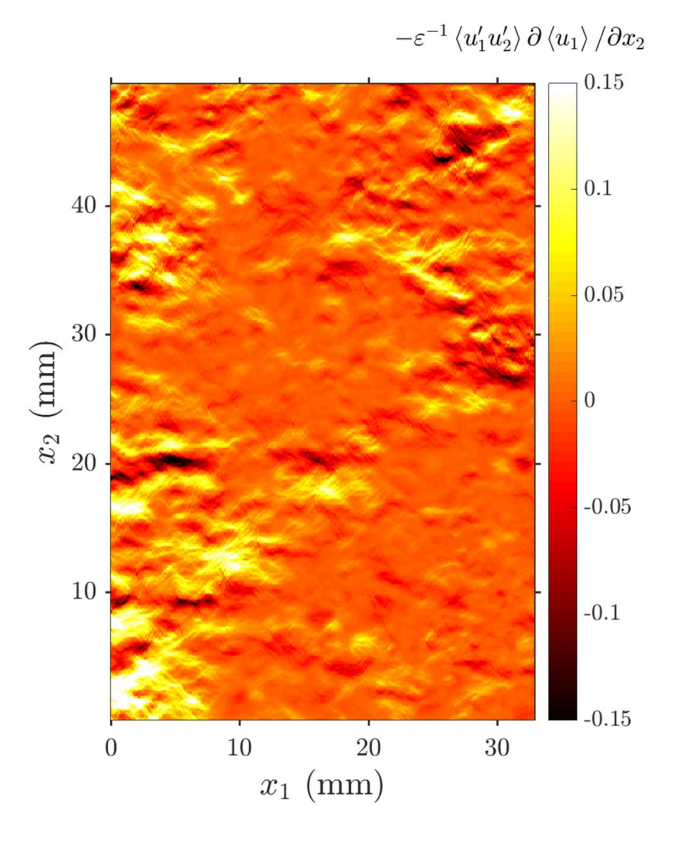


Fig. 5 Spatial map of TKE production term $-\langle u_1'u_2'\rangle \partial \langle u_1\rangle /\partial x_2$ normalized by ε for the 29 W case

The Taylor microscale based on the longitudinal autocorrelation function λ_f and the associated Reynolds number Re_{λ} are computed using the following relationships derived for ideal isotropic turbulence.

$$\lambda_f = \left(\frac{10\nu q^2}{\varepsilon}\right)^{1/2}, Re_{\lambda} = \frac{\left(q^2/3\right)^{1/2}\lambda_f}{\nu} \tag{13}$$

The maximum attained Reynolds number is $Re_{\lambda} = 240$, with a corresponding Taylor microscale of 4.9 mm. Over the range of jet power settings measured, Re_{λ} appears to follow a power-law behavior, as suggested by Eq. (5). In Fig. 6, Re_{λ} is plotted as a function of P with a trend line suggesting the scaling exponent for P is 0.42. This is significantly higher than the scaling exponent of 1/6 given by Eq. (5), which may indicate a strong increase in the actuator efficiency with P over this range.

Finally, the integral length scale is obtained from Eq. (14).

$$L = \frac{(q^2/2)^{3/2}}{\varepsilon} \tag{14}$$

The integral length scale varies from 68.3 to 81.7 mm with no discernible trend with the jet power setting, as expected,



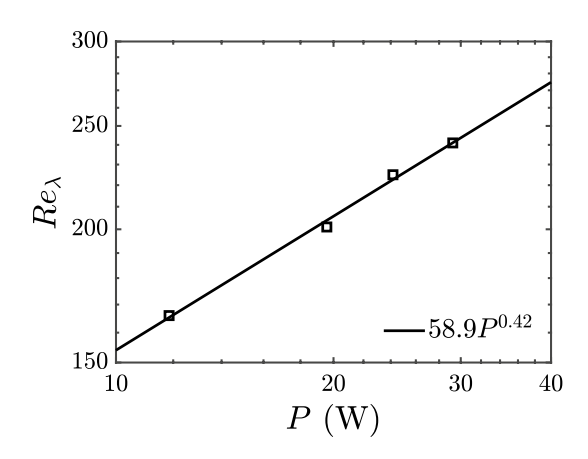


Fig. 6 Reynolds number Re_{λ} as a function of the applied jet actuator power P

since the jet diameter and driving frequency are the same in all measurements.

3.2 Two-point velocity statistics

The dissipation rate ε is estimated using the second-order structure function fitting method, which has been shown to be the most robust technique for PIV data, compared to other existing methods (de Jong et al. 2008). Briefly, the method relies on Kolmogorov's second similarity hypothesis (Kolmogorov 1941), which states that the longitudinal second-order structure function $D_{ii}(r)$ follows the power-law,

$$D_{ii}(r) = C_2(Re_{\lambda})(\varepsilon r)^{2/3},\tag{15}$$

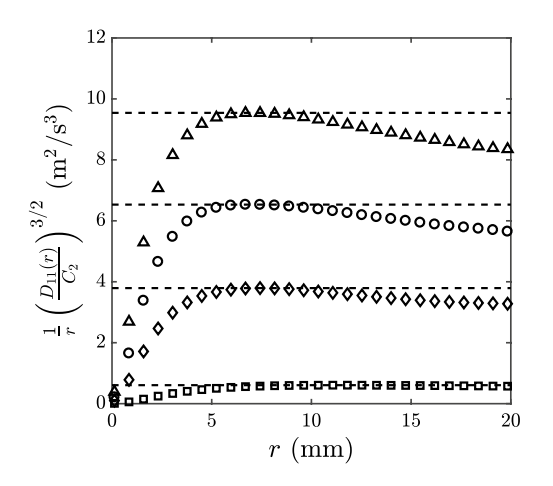
when r lies in the inertial subrange. The longitudinal secondorder structure function is a two-point velocity statistic that can be computed from the PIV data using Eq. (16).

$$D_{ii}(r) = \overline{\langle [u_i(x_i + r, x_i) - u_i(x_i, x_i)]^2 \rangle}$$
 (16)

Once the inertial subrange is identified, the dissipation rate can be inferred from a combination of Eqs. 15 and 16. For large Re_{λ} , the constant $C_2=2.13$ is considered universal (Sreenivasan 1995). Over the range of Re_{λ} investigated here, however, it is not safe to assume C_2 is fixed. We rely on the forced isotropic turbulence DNS of Yeung and Zhou (1997) to determine the appropriate value of $C_2(Re_{\lambda})$. Since the calculation of ε is implicit (Re_{λ} and C_2 depend on ε) the values for ε , Re_{λ} , and C_2 are solved simultaneously in an iterative manner, with $C_2=2.13$ taken as the starting value.

By rearranging Eq. (15), it is convenient to define the compensated structure function, $r^{-1}(D_{ii}(r)/C_2)^{3/2}$, and identify the value of r at which a plateau is reached as the start of the inertial subrange. The compensated structure functions computed in the x_1 and x_2 directions, $r^{-1}(D_{11}(r)/C_2)^{3/2}$ and $r^{-1}(D_{22}(r)/C_2)^{3/2}$, respectively, are plotted in Fig. 7. The converged estimates for the dissipation rates are indicated by the horizontal dashed lines. Fig. 7 highlights the anisotropy that exists for spatial scales in the inertial subrange, as the calculation in the x_2 direction gives consistently higher estimates for the dissipation rate. Knutsen et al. (2020) showed that scale-space anisotropy is important in setting the dynamics of the energy cascade. The discrepancy in the plateau, when comparing the left and right plots of Fig. 7, can be as high as 18%. As a final estimate for the dissipation rate, we use the weighted average defined by Eq. (10), and the values are reflected in Table 3.

An alternative two-point velocity statistic which is often used to characterize the isotropy of intermediate scales is the autocorrelation function. The longitudinal and transverse autocorrelation functions may be computed from the PIV velocity fields according to Eqs. 17 and 18, respectively.



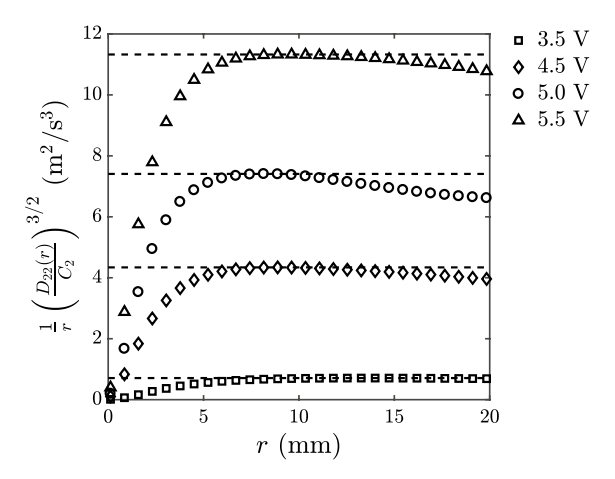


Fig. 7 Compensated longitudinal structure functions computed in the x_1 direction (left) and the x_2 direction (right) for each synthetic jet actuator voltage. The horizontal dashed lines indicate the corresponding dissipation rate estimate



$$F_{ii}(r) = \overline{\langle u_i'(x_i + r, x_i)u_i'(x_i, x_i)\rangle} / \overline{u_{i,\text{rms}}}^2$$
(17)

$$G_{ii}(r) = \overline{\langle u_i'(x_i, x_j + r)u_i'(x_i, x_j)\rangle/\overline{u_{i,\text{rms}}}^2}$$
(18)

A consequence of isotropy results in the following relationship between $F_{ii}(r)$ and $G_{ii}(r)$.

$$G_{ii}(r) = F_{ii}(r) + \frac{1}{2}r\frac{dF_{ii}}{dr}$$
 (19)

It can be shown that the inverse relationship is given by

$$F_{ii}(r) = \frac{2}{r^2} \int_0^r r' G_{ii}(r') dr'.$$
 (20)

Both longitudinal and transverse autocorrelation functions are computed directly from the PIV velocity fields. The directly computed functions $F_{11}(r)$ and $F_{22}(r)$, plotted in Fig. 8, align closely together. To further test the isotropy assumption, we also compute $G_{11}(r)$ and $G_{22}(r)$ and apply Eq. (20) to infer $F_{11}(r)$ and $F_{22}(r)$. The inferred autocorrelation functions also align closely with their directly measured counterparts, indicating that the isotropy assumption built into Eq. (20) is valid. We also verify that the curvature of the autocorrelation function at r=0 is in agreement with the estimate of the Taylor microscale obtained at 29 W jet power, $\lambda_f=4.9$ mm, by plotting the polynomial expression $p(r)=1-(r/\lambda_f)^2$.

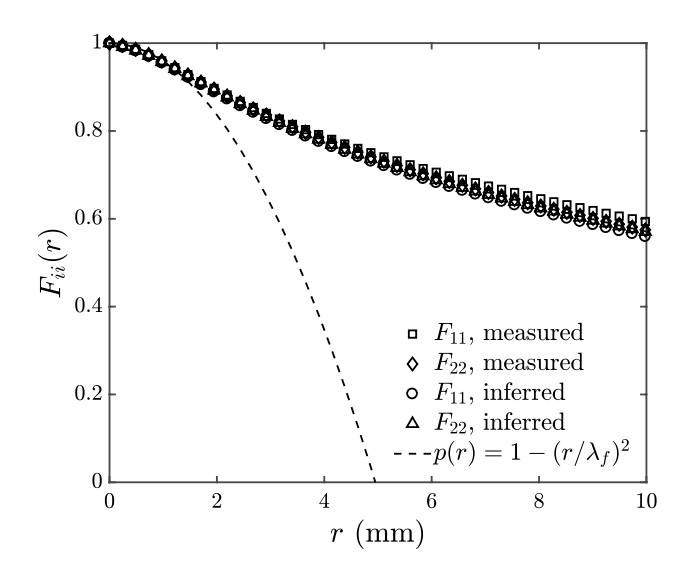


Fig. 8 Longitudinal autocorrelation function computed in the x_1 and x_2 directions for the 29 W jet power setting. The measured autocorrelation functions are computed using Eq. (17), and the inferred autocorrelation functions are obtained from Eqs. 18 and 20

3.3 Energy spectra

The longitudinal velocity power spectra $E_{11}(k_1)$ and $E_{22}(k_2)$ are obtained as a further check of the turbulence isotropy. These are computed by first windowing the velocity component in the direction of interest using a Hanning function, followed by the FFT algorithm, and then averaging over space in the remaining direction. For wavenumbers k_i within the inertial subrange, the spectra should exhibit power-law behavior, according to Eq. (21).

$$E_{ii}(k_i) = 0.53\varepsilon^{2/3}k_i^{-5/3} \tag{21}$$

In Fig. 9, the compensated longitudinal velocity power spectra, $[E_{11}(k_1)k_1^{5/3}/0.53]^{3/2}$ and $[E_{22}(k_2)k_2^{5/3}/0.53]^{3/2}$, are plotted as a function of the normalized wavenumber for the 29 W experiment. The horizontal dashed line corresponds to the dissipation rate estimate obtained by the structure function fitting method described in Sect. 3.2. The compensated spectra should plateau towards the left side of Fig. 9, corresponding to wavenumbers at the start of the inertial subrange, but the PIV viewing window is too small to fully capture the behavior of the larger scales. Nevertheless, the values appear to asymptote to the dissipation rate value previously determined in Sect. 3.2. For the higher wavenumbers, the spectra align reasonably well, providing further evidence for the turbulence isotropy. The slight deviation in the right-side tails of the spectra can be attributed to random errors in the PIV vector fields.

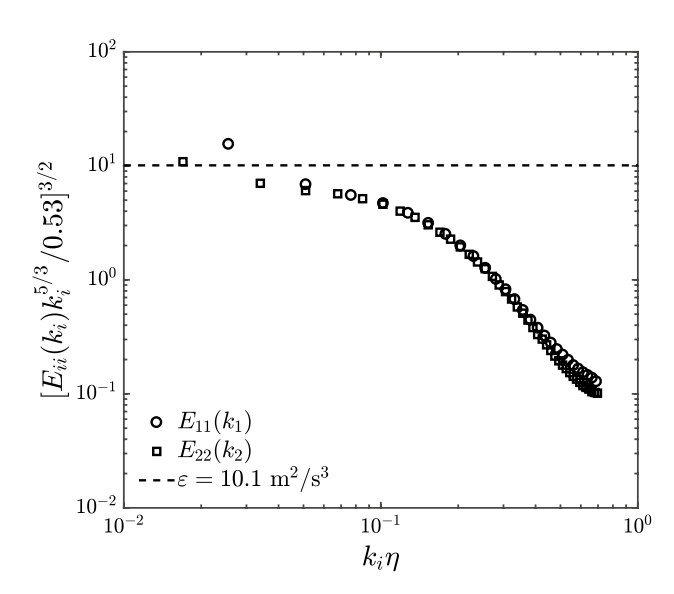


Fig. 9 Compensated longitudinal velocity power spectra for the 29 W jet power setting. The horizontal dashed line indicates the dissipation rate estimate obtained from the structure function fitting method



209 Page 10 of 11 Experiments in Fluids (2021) 62:209

4 Conclusion

Since its earliest conception, the closed turbulence box design has made it feasible to study the role of turbulence in numerous applications. One such application, the agglomeration of inertial particles, has prompted the fabrication of a new turbulence tower facility. The turbulence tower sustains a column of homogeneous and nearly isotropic turbulence along its central axis using arrays of synthetic jets and operates without a net flow through the chamber. The turbulence is characterized using 2D PIV at various locations in the tower to quantify the homogeneity and isotropy of the velocity fluctuations and statistics. The synthetic jet power setting can be varied from 12 and 29 W, with Re_{λ} reaching up to 240.

The homogeneous region extends roughly 1.0 m, or 13 integral length scales, in the vertical direction and at least 1.7 cm from the central axis of the tower. Further off-axis PIV measurements would be required to better quantify the spatial homogeneity in this direction.

The degree of isotropy is quantified in a variety of ways, including the rms velocity ratio, longitudinal structure functions, autocorrelations, and velocity power spectra. These metrics indicate that the turbulence is close to isotropic in the small scales with some large-scale anisotropy occuring near the primary stagnation points, where the local rms velocity ratio $u_{1,\text{rms}}/u_{2,\text{rms}}$ reaches up to 1.33. The compensated second-order longitudinal structure functions, used to estimate the dissipation rate, are up to 18% different when computed in different directions, indicating that the large-scale anisotropy also leaks into the inertial subrange. In contrast, the longitudinal autocorrelation functions $F_{11}(r)$ and $F_{22}(r)$ show good agreement with each other and with isotropic turbulence theory within the small to intermediate scales. The velocity power spectra similarly reveal a high degree of isotropy for large wavenumbers, but the limited PIV viewing window prevents full comparisons for wavenumbers in the inertial subrange.

The time-averaged velocities are small relative to the fluctuating velocities but still significant. The mean stagnation point that arises as a consequence of jet impingement is capable of producing TKE via the mean shear mechanism. However, the product of the Reynolds stress component $\langle u'_1 u'_2 \rangle$ with the mean velocity gradients is small relative to the dissipation rate, so that TKE production is not a significant source of the large scale anisotropy.

Based on the present turbulence tower design, we offer one main guideline for future designs. To reduce mean flows around the jet stagnation points, the chamber width 2w could be increased to the point where the jet half-width a distance w from the jet orifice is at least as large as the

inter-jet spacing. More powerful jets, or a greater number of jets, would be needed to offset the reduction in ε caused by the increase in w. Based on the scaling arguments presented, a two-fold increase in the chamber half-width would necessitate a four-fold increase in the jet actuator power to hold the Kolmogorov length scale constant.

Acknowledgements This material is based upon work supported by the National Science Foundation under Grant EAR-1756068.

References

- Bellani G, Variano EA (2014) Homogeneity and isotropy in a laboratory turbulent flow. Exp Fluids 55(1), 1–12
- Brown R, Bonadonna C, Durant A (2012) A review of volcanic ash aggregation. Phys Chem Earth 45–46:65–78
- Carter D, Petersen A, Amili O, Coletti F (2016) Generating and controlling homogeneous air turbulence using random jet arrays. Exp Fluids 57(12):189
- Comte-Bellot G, Corrsin S (1966) The use of a contraction to improve the isotropy of grid-generated turbulence. J of Fluid Mech 25(4), 657–682
- de Jong J, Cao L, Woodward SH, Salazar JPLC, Collins LR, Meng H (2008) Dissipation rate estimation from PIV in zero-mean isotropic turbulence. Exp Fluids 46(3):499
- De Silva IPD, Fernando HJS (1994) Oscillating grids as a source of nearly isotropic turbulence. Phys Fluids 6(7), 2455–2464
- Dou Z, Pecenak ZK, Cao L, Woodward SH, Liang Z, Meng H (2016) PIV measurement of high-Reynolds-number homogeneous and isotropic turbulence in an enclosed flow apparatus with fan agitation. Meas Sci Techno 27(3):35305
- Goepfert C, Marié JL, Chareyron D, Lance M (2010) Characterization of a system generating a homogeneous isotropic turbulence field by free synthetic jets. Exp Fluids 48(5), 809–822
- Good G, Ireland P, Bewley G, Bodenschatz E, Collins L, Warhaft Z (2014) Settling regimes of inertial particles in isotropic turbulence. J Fluid Mech 759
- Hwang W, Eaton JK (2004) Creating homogeneous and isotropic turbulence without a mean flow. Exp Fluids 36(3), 444–454
- Johnson BA, Cowen EA (2020) Sediment suspension and bed morphology in a mean shear free turbulent boundary layer. J of Fluid Mech 894:A8
- Knutsen AN, Baj P, Lawson JM, Bodenschatz E, Dawson JR, Worth NA (2020) The inter-scale energy budget in a von Kármán mixing flow. Journal of Fluid Mechanics 895:A11
- Kolmogorov AN (1941) The local structure of turbulence in incompressible viscous fluid for very large Reynolds numbers. CR Acad Sci USSR 30:301–305
- Pope SB (2000) Turbulent flows. Cambridge: Cambridge Univ. Press Roth GI, Katz J (2001) Five techniques for increasing the speed and accuracy of PIV interrogation. Meas Sci Techno 12(3), 238–245
- Saffman PG, Turner JS (1956) On the collision of drops in turbulent clouds. J of Fluid Mech 1(1), 16–30
- Smoluchowski M (1917) Versuch einer mathematischen Theorie der Koagulationskinetik kolloider Lösungen. Z Phys Chem 92:129–168
- Sreenivasan KR (1995) On the universality of the Kolmogorov constant. Phys Fluids 7(11), 2778–2784
- Sundaram S, Collins LR (1997) Collision statistics in an isotropic particle-laden turbulent suspension. Part 1. Direct numerical simulations. J of Fluid Mech 335:75–109



- Yeung PK, Zhou Y (1997) Universality of the Kolmogorov constant in numerical simulations of turbulence. Phys Rev E 56(2), 1746–1752
- Zimmermann R, Xu H, Gasteuil Y, Bourgoin M, Volk R, Pinton JF, Bodenschatz E (2010) The Lagrangian exploration module: An apparatus for the study of statistically homogeneous and isotropic turbulence. Rev Sci Instrum 81(5):55112

Publisher's Note Springer Nature remains neutral with regard to jurisdictional claims in published maps and institutional affiliations.

